An SOC Based Adaptive Energy Management System for Hybrid Energy Storage System Integration to DC Grid

Sanjib Kumar Mitra, Student Member, IEEE, and Srinivas Bhaskar Karanki, Senior Member, IEEE

The authors are with the School of Electrical Sciences, Indian Institute of Technology Bhubaneswar, Bhubaneswar 752050, India (e-mail: skm19@iitbbs.ac.in; skaranki@iitbbs.ac.in).

This work was financially supported by the Department of Science and Technology (DST), India and the European Union's Horizon 2020 Research and Innovation Program through the RE-EMPOWERED Project under Grant Agreement No DST/TMD/INDIA/EU/ILES/2020/50(c) and 101018420 respectively.

Digital Object Identifier 10.1109/TIA.2022.3211248

An SOC Based Adaptive Energy Management System for Hybrid Energy Storage System Integration to DC Grid

Sanjib Kumar Mitra, *Student Member, IEEE,* and Srinivas Bhaskar Karanki, *Senior Member, IEEE*

***Abstract*—In this paper, an efficient adaptive energy management strategy (EMS) is presented for a hybrid energy storage system (HESS) application to compensate power fluctuation. The HESS consists of a battery and super-capacitor, which are integrated into the DC grid using a modified triple active bridge converter (m-TAB). The conventional EMS uses a low pass filter (LPF) to distribute high and low-frequency components of power. However, the time constant of the LPF is fixed throughout the process, which discharges the battery at the same rate even near the low state of charge (SOC) region. This increases the degradation rate of the battery. The proposed EMS employs an adaptive time constant LPF-based power allocation method to distribute the total power between the energy storage devices. The adaptive feature of the EMS changes the power distribution ratio dynamically to increase the utilization of the super-capacitor and battery operation time, thereby enhancing the life cycle. The proposed EMS is simulated in MATLAB/SIMULINK platform with the m-TAB converter, and the results are compared with the conventional EMS to prove its superiority. The system is also tested on an experimental prototype of 500W for different test cases, and the outcomes are presented to support the proposed EMS.**

***Index Terms*—hybrid energy storage system, HESS, energy management system, EMS, adaptive control**

I. Introduction

Renewable energy sources (RES) are the future of modern power systems due to the sharp fall in fossil fuel reserves and the continuous rise in power demand [1]–[3]. But, the dependency of these RES on uncontrollable weather conditions makes them unpredictable [4], [5]. This feature poses a challenge in maintaining the power quality of the system. The problem can be resolved by using energy storage devices (ESD) as a reserve in the system [6], [7]. Conventionally a battery energy storage (BES) with high energy density is used for this purpose, but it can not provide power rapidly due to slow operation time. A super-capacitor (SC) with high power density is used along with BES to solve this issue. The SC provides the transient power, whereas the steady state power is provided by the BES [8]. This methodology is generally achieved by connecting multiple ESDs with different power densities [9]–[11]. However, this method requires more converters, increasing the control structure's complexity and the overall system's cost. In this scenario, a multi-port DC-DC converter with a modular structure is preferable.

This paper was produced by the IEEE Publication Technology Group. They are in Piscataway, NJ.

Manuscript received April 19, 2021; revised August 16, 2021.

Over the years of research, several multi-port DC-DC converters have been discussed [12]. It is observed that an isolated triple active bridge (TAB) converter is most suitable for the application mentioned above due to the following benefits:

- modular structure
- electrically isolated input and output ports
- wide range of voltage gain
- no switching loss over a wide range of operation
- high efficiency
- compact size due to high-frequency switching

The phase shift angle decides the power flow from the energy storage devices between the voltages of the different ports of the TAB converter. These phase shift angles are provided by the controller.

The researchers have explored different types of controllers for TAB converters. Most of them focus on current controlling using two loop controls where voltage and current feedback are necessary. Moreover, the generated current references have to be decoupled from each other to distribute the currents properly. Such decoupling methods and associated controllers are discussed in [13]–[17]. These methods decouple the active power between all the converter ports so that they work as multiple independent dual active bridge converters and efficiently distribute the power between all ports of the converters. However, they require a detailed analysis of the converter as they mostly use PI controllers in tracking the references. An error in the estimation of the converter model will degrade the system performance considerably. Moreover, for the hybrid energy storage system application, the power demand needs to be distributed beforehand to generate the reference currents using some splitting technique, which has not been discussed in the literature. Alternately, a flatness-based non-linear controller has been implemented in [18], [19] with slew rate control for HESS application with fuel cell and super-capacitor. Although the controller's performance is satisfactory, it requires a high-end processor for implementation due to its complex design and non-linear calculations. An adaptive controller is well suited to eliminate the requirement of detailed state and parameter information and reduce complexity. This adaptive controller is implemented in [20] for a dual active bridge converter with a single ESD. However, for HESS application, the actuating signal has to be distributed using some splitting methods. Hence, it is important to investigate a proper power splitting mechanism to ensure the reliability of the entire system.

The battery stress and degradation depend on temperature, charge/discharge rate, depth of discharge, and charge cycle intervals [21]. Batteries are generally designed for a particular range of operations. Overcharging/discharging causes degradation of the life cycle of the battery. Moreover, the degradation rate in the acceptable range is also a function of the charge/discharge rate [21]. A relation between capacity fade percentage, cycle number, and discharge rate is studied in [22], which confirms that as the cycle number increases, the capacity fade percentage increases with an increase in discharge rate. So, it is crucial to control the charge/ discharge rate to improve the battery life cycle. A fuel cell and super-capacitor system have been described in [23], using a triple active bridge converter to maintain a fixed output voltage and constant fuel cell power. In [24], a fuel cell, battery, and ultra-capacitor system are demonstrated for a triple half-bridge converter with individual/combined peak power and state of charge (SOC) control strategy in a vehicle system. However, as the fuel cell here is the primary source, the energy storage devices attain a specified SOC as given by the user as per the vehicle's speed. In the present system under study for HESS application, the battery SOC may experience a constant change, and SOC control will be inefficient. A conventional energy sharing strategy [8] has been employed for a current fed triple active bridge converter in [25]. In this work, a simple low pass filter has been used to differentiate between the low and high-frequency components of the power fluctuation. However, the SOC of ESDs is not considered to generate the reference currents. Hence, the charge/discharge rate of the battery remains fixed even at the marginal SOC values, thereby over/underutilizing the storage devices. A master/slave control for a parallel connected dual active bridge converters is proposed in [26] to distribute power among multiple battery storage. However, it experiences voltage balancing issues, higher current stress, and low efficiency, as discussed in [27]. Alternately, a fuzzy logic-based energy management system is proposed in [28] for shipboard applications where the storage devices charge/discharge at a different rate based on their SOCs. However, the power distribution between the battery and super-capacitor is still decided by a low pass filter with a fixed time constant when the SOCs are within their limit. A similar approach using a high-pass and low-pass filter was utilized in [29] along with a SOC control technique for a quadruple active bridge converter. These rule-based EMS methods rely entirely on human expertise and preselected priorities. Hence, their performance depends on tuning accuracy and rule design. Several research have also been carried out in different adaptive LPF methods [30]–[33]. A predictive set point modulation-based EMS is described in [30]. In this work, the LPF cut-off frequency is changed based on the SOC of the super-capacitor and FFT analysis of the power spectrum to change the battery discharge rate. Although the method ensures the long-term operation of the super-capacitor, the SOC of the battery was not taken into account to decide whether it can provide sufficient power. Moreover, the computation complexity of this method requires high-end processors for better performance. In [31], the cut-off frequency of the LPF is varied based on the output of the DC-link voltage and the super-capacitor (SC) state of charge (SOC). The time constant of the LPF is determined empirically by a look-up table (LUT) with three fixed time constants. As this method uses a rule-based frequency splitting, its efficiency depends on the design of the rules. Moreover, the authors did not consider the SOC of the battery to determine the time constant, which is essential to preserve the battery life. In [32], the authors have considered an improved particle swarm optimization (IPSO) based variable time constant LPF strategy. However, the authors did not consider the power limits of the energy storage devices. In [33], the authors have considered the SOC of both the ESDs to pre-allocate the power references. Then a windowed FFT-based power spectrum is designed to calculate the split frequency of the LPF. Although the method is efficient, the SC can still be in charging mode even after reaching 100% SOC. Also, the pre-allocation of power is dependent on the power demand. Hence, the controller experiences delay in calculating and distributing the battery and SC power references. Hence, based on the literature, it can be inferred that the most widely used technique found in the literature uses a low-pass/high-pass filter to allocate the actuating signal. However, these techniques do not consider the SOC of both the ESDs to allocate the power between the battery and super-capacitor.

Motivated by the issue mentioned above, a SOC-based adaptive energy management system (EMS) for a modified triple active bridge converter is presented in this article. The proposed technique has the following salient features:

- it can allocate power in the HESS based on the SOC of both the ESDs.
- it improves the SC utilization while maintaining the stability of the DC link for long-term application.
- it improves battery lifetime by changing charge/discharge rate dynamically.

As compared to the conference paper [34], the significant contributions of this manuscript are as follows:

1) operational explanation of the HESS control structure.
2) design of SOC-based adaptive EMS with a varying time constant for HESS power allocation.
3) extensive experimental analysis for different test conditions.

The remainder of this manuscript is organized as follows. In Section II, a description of the circuit and control framework has been discussed. The SOC-based adaptive EMS is described in Section III. Section IV describes the simulation and experimental results. Finally, a conclusion of the proposed work has been drawn in Section V.

II. TOPOLOGY DESCRIPTION AND CONTROL FRAMEWORK

A conventional triple active bridge converter consists of three H-bridges and one three-windings high-frequency transformer (HFT). The low voltage (LV) side bridges are connected to a battery (V_{batt}) and super-capacitor (V_{sc}), which are galvanically isolated, and the high voltage (HV) side bridge is connected to the DC link (V_{dc}) of the micro-grid. The HV side bridge switches experience high voltage stress which

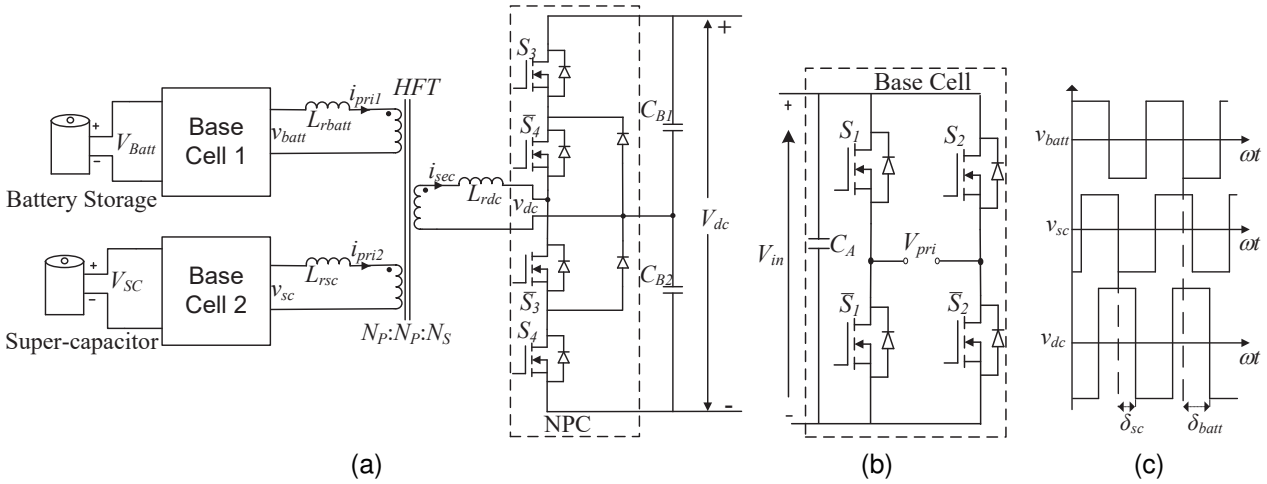

Fig. 1. (a) HESS integrated system, (b) Base Cell, (c) HFT voltage waveforms.

increases their rating. In this work, a modified TAB converter (m-TAB), as shown in Fig. 1a, is implemented to reduce the voltage stress of HV switches and double the voltage gain by connecting them to a neutral point clamped (NPC) structure working as a voltage doubler [34]. The LV side base cells are shown in Fig. 1b. The inductors $L_{r_{batt}}$, $L_{r_{sc}}$ and $L_{r_{dc}}$ are leakage inductance of the HFT. In practice, these values might be equal or unequal. Depending on their values and switching method, zero voltage switching is achieved. The DC link is formed by combining the capacitors C_{B1} and C_{B2}.

The LV side bridges and HV side NPC structure generate three high-frequency voltage waveforms, as shown in Fig 1c, and the phase shift between them determines the power flow in individual ports. The phase shift angle between the NPC and battery side bridge voltage is termed δ_{batt}. Similarly, the phase shift angle between NPC side and SC side bridge voltage is denoted as δ_{sc}. The equivalent circuit expressed as delta model is shown in Fig. 2 where $L_{rbatt-dc}$, $L_{rbatt-sc}$ and L_{rsc-dc} are the effective inductance between the corresponding ports. The power transfer P_{a-b} (from $port-a$ to $port-b$) between any two port, considering the third port open are expressed as (1).

$$\left.\begin{aligned} P_{batt-dc} &= \frac{N_p}{N_s}\frac{V_{dc}V_{batt}\delta_{batt}(\pi-|\delta_{batt}|)}{4\pi\omega\left(L_{r_{batt}}+L_{r_{dc}}\right)} \\ P_{sc-dc} &= \frac{N_p}{N_s}\frac{V_{dc}V_{sc}\delta_{sc}(\pi-|\delta_{sc}|)}{4\pi\omega\left(L_{r_{sc}}+L_{r_{dc}}\right)} \\ P_{batt-sc} &= \frac{N_p}{N_p}\frac{V_{batt}V_{sc}(\delta_{batt}-\delta_{sc})(\pi-|(\delta_{batt}-\delta_{sc})|)}{4\pi\omega\left(L_{r_{batt}}+L_{r_{sc}}\right)} \end{aligned}\right\} \quad (1)$$

where, $N_p : N_p : N_s$ = turns ratio of the HFT and ω is the angular switching frequency. However, for the HESS application, SC connected port will never be open to cater to the additional power demand. Hence, it is required that all three port powers are expressed separately [13]. From the delta model shown in Fig. 2 and using the superposition theorem, the individual port powers are expressed as given by (2)

$$\left.\begin{aligned} P_{batt} &= \frac{\begin{array}{r}\frac{N_p}{N_s}V_{dc}V_{batt}\delta_{batt}\left(\pi-\delta_{batt}\right)L_{r_{sc}} \\ +V_{sc}V_{batt}\left(\delta_{batt}-\delta_{sc}\right)\left(\pi-\delta_{batt}+\delta_{sc}\right)L_{r_{dc}}\end{array}}{4\pi\omega\left(L_{r_{batt}}L_{r_{dc}}+L_{r_{batt}}L_{r_{sc}}+L_{r_{sc}}L_{r_{dc}}\right)} \\ P_{dc} &= \frac{\begin{array}{r}\frac{N_p}{N_s}V_{dc}V_{batt}\delta_{batt}\left(\delta_{batt}-\pi\right)L_{r_{sc}} \\ +\frac{N_p}{N_s}V_{dc}V_{sc}\delta_{sc}\left(\delta_{sc}-\pi\right)L_{r_{batt}}\end{array}}{4\pi\omega\left(L_{r_{batt}}L_{r_{dc}}+L_{r_{batt}}L_{r_{sc}}+L_{r_{sc}}L_{r_{dc}}\right)} \\ P_{sc} &= \frac{\begin{array}{r}V_{sc}V_{batt}\left(\delta_{sc}-\delta_{batt}\right)\left(\pi-\delta_{batt}+\delta_{sc}\right)L_{r_{dc}} \\ +\frac{N_p}{N_s}V_{dc}V_{sc}\delta_{sc}\left(\pi-\delta_{sc}\right)L_{r_{batt}}\end{array}}{4\pi\omega\left(L_{r_{batt}}L_{r_{dc}}+L_{r_{batt}}L_{r_{sc}}+L_{r_{sc}}L_{r_{dc}}\right)} \end{aligned}\right\} \quad (2)$$

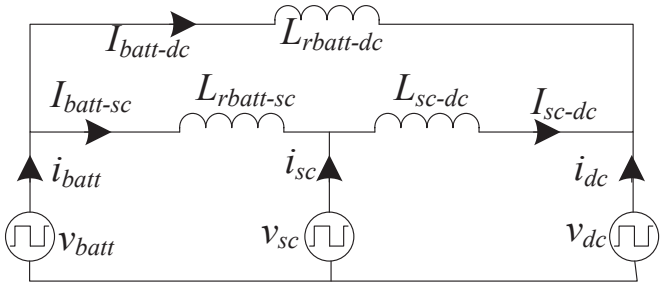

Fig. 2. Equivalent Δ-model of m-TAB

From (2) the relations between P_{batt} and δ_{batt}, δ_{batt} and δ_{sc} at steady state can be solved with the conditions $P_{batt} = -P_{dc} = P$ and $P_{sc} = 0$. An example operating condition is shown in Fig. 3. The corresponding circuit parameter used is given in Table I. It is observed from Fig. 3a for a power flow condition of $273W$ from battery side to grid side; there are two solutions of δ_{batt} out of which the lower value $(9°)$ is selected for reducing peak current and conduction loss. For this specified power the value of δ_{sc} is found from Fig. 3b as $2.96°$.

During a change in power flow, δ_{batt} will also vary accordingly. However, this change should not be instantaneous for improving battery life cycle for the HESS application. So,

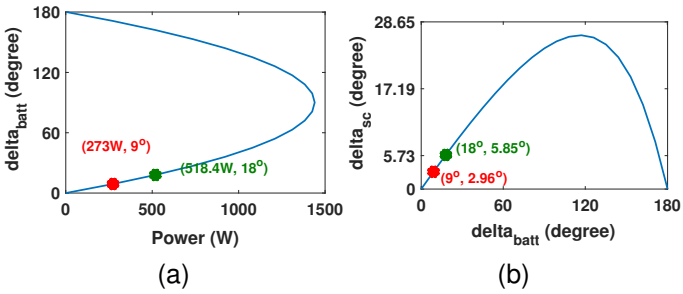

Fig. 3. Relationship curve between (a) Power and δ_{batt}, (b) δ_{batt} and δ_{sc}.

TABLE I
SYSTEM PARAMETERS

System Parameter	Value
Nominal Power rating	500 W
Battery rating	48 V, 10Ah
SC rating	48 V, 19.3F
Nominal DC link Voltage	249.6 V
Inductor (L_r)	1.54 μH
Output Capacitor (C)	500 μF
Turns ratio of HFT	1:2.5
Switching Frequency	50 kHz
Adaptation gain (γ)	0.5
Reference model parameter (a_m, b_m)	580
Initial LPF Time constant ($T_{previous}$)	10s
Time constant step change (ΔT)	10s

this additional change is provided by adjusting δ_{sc}. As can be seen from Fig. 3a for delivering 518.4W power to the grid side, $\delta_{batt} = 18°$ and $\delta_{sc} = 5.85°$ at steady state. But, during this step change δ_{batt} remains unaltered at $9°$ and increases gradually to reach the new value of $18°$, whereas, δ_{sc} jumps to $15.04°$ $(= 18° - 2.96°)$ and gradually decreased to $5.85°$. This variation of phase shift angles is provided by the adaptive energy management system.

III. SOC BASED ADAPTIVE ENERGY MANAGEMENT SYSTEM

The primary objective of the EMS is to maintain the DC link voltage to its desired value and adequately allocate the power between the battery and SC. As a higher power density device, the SC addresses the transient state, and the battery provides long-term power due to its higher energy density. However, the conventional EMS as discussed in [13]–[19] require a detail knowledge of the system information. The performance of the EMS depends on the modeling accuracy of the converter, present SOC of the ESDs, and design of the power split rules. Overall the system becomes complex and sensitive to the operating point and parameter changes. To overcome these problems, an adaptive EMS is designed for the TAB converter that monitors the present SOC of the ESDs and distributes the power between the ESDs. The proposed EMS uses a model reference adaptive power controller (MRAPC) for voltage control followed by an LPF with a dynamically variable time constant. The MRAPC does not require detailed system knowledge to operate. Moreover, it is robust to the system parameter changes, which emphasize the adaptive nature of the controller. The LPF is also adaptive as its time constant is dynamically changing depending on the SOC of ESDs in online mode.

The proposed EMS is divided into two stages, (1) model reference adaptive power controller for estimating steady-state δ_{batt}, and (2) SOC-based power allocation between the ESDs.

A. Model Reference Adaptive Power Controller (MRAPC)

In this work, a model reference adaptive controller is designed to generate a proper steady state $\delta_{ss} = \delta_{batt}$ (with SC port as open) to control the DC link voltage.

The control schematic is shown in Fig. 4. The reduced order model of the converter system with SC port open is expressed in (3) where a_p and g are considered unknown for this work and depend on system parameters [20], [34].

$$\frac{dV_{dc}}{dt} = -a_p V_{dc} + g \tag{3}$$

Equation (4) provides a first-order reference model for the MRAC controller. The parameters x_m and $r(t)$ are output voltage and input reference voltage, respectively. The behavior of this reference model is determined by the parameters a_m and b_m, which are positive real numbers. The output of the plant transfer function is compared with the output of this reference model to estimate the control input δ_{ss}. The input $r(t)$ to the reference model is generated by a droop controller to maintain the voltage deviation within 5% of nominal voltage.

$$\frac{dx_m}{dt} = -a_m x_m + b_m r(t) \tag{4}$$

The error $e_m = V_{dc} - x_m$ converges to zero asymptotically. The control input δ_{ss} to the converter is calculated from the control law as expressed in (5).

$$u(t) = \sin[\delta_{ss}] = a_r(t) r(t) + a_y(t) V_{dc} \tag{5}$$

where $a_r(t)$ and $a_y(t)$ denote adaptation parameters and are obtained from the adaptation law as

$$\left.\begin{aligned} \tfrac{da_r(t)}{dt} &= -sign(g)\gamma e_m r(t) \\ \tfrac{da_y(t)}{dt} &= -sign(g)\gamma e_m V_{dc} \end{aligned}\right\} \tag{6}$$

Here, γ is a positive real adaptation gain and $sign(g)$ is the sign of g. This δ_{ss} is split in δ_{batt} and δ_{sc} to support HESS application. Initially δ_{sc} will be the difference $(\delta_{ss} - \delta_{batt})$ and it will gradually decrease to a value where $P_{sc} = 0$.

B. SOC based Power Allocation Method

Fig. 5 shows the conventional power allocating technique [8]. The sudden change of power reference consists of a high and low-frequency component. Hence, the total reference power P_{HESS} is passed through a low pass filter (LPF) to pass only low-frequency components. The output of the LPF P_{Batt} is then subtracted from P_{HESS} to generate the P_{SC}. The output P_{Batt} and P_{SC} act as the reference input to the current controllers to calculate δ_{batt} and δ_{sc}. However, this method keeps the LPF time constant fixed for the entire zone of operation, which is decided by the SOCs of the ESDs.

Generally, the SOC operation zones are divided into two or three parts, and a separate time constant is assigned for each part. This method still does not properly utilize the SC's capacity as the time constant is changed discretely and not dynamically. As a solution, a SOC-based dynamic variable time constant LPF is proposed in this article to utilize the SC properly.

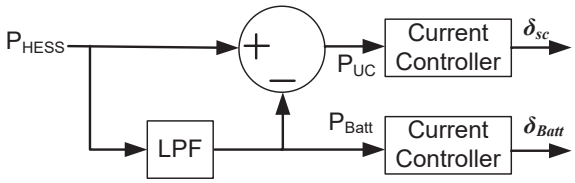

Fig. 5. Power split using conventional method.

The battery and super-capacitor safe operation limits are different. Generally, a Li-ion battery is operated within $30\% - 90\%$ of the SOC limit for safety. However, a super-capacitor is safe to operate from $40\% - 95\%$ of SOC limit [35]. Due to this mismatch in the safety zone of operation, normalization of the SOC is required and calculated as

$$y_{norm}(t) = \frac{y(t) - y_{min}}{y_{max} - y_{min}}, \qquad 0 \le y_{norm} \le 1 \tag{7}$$

where, $y(t)$ is the SOC at the instant t. The normalized, minimum, and maximum allowable SOC for the safe operation of ESD are denoted by subscripts $norm$, min, and max, respectively. The idea of the proposed technique is that when $y_{norm}(t)$ is near to 1, the discharge rate of that ESD will be strong, whereas it will be weak when $y_{norm}(t)$ is close to 0. At the start the time constant is denoted by $T_{initial}$. Depending on the normalized SOC value of the energy storage devices, the time constant of LPF is dynamically changed as expressed in (8)

$$T = T_{initial} + \alpha(t)\,\Delta T \tag{8}$$

where ΔT is the small positive variation in T and $\alpha(t)$ is an adaptive parameter calculated as follows

$$\alpha(t) = \begin{cases} 1 - y_{norm_{Batt}}(t) & y_{norm_{Batt}}(t) < y_{norm_{sc}}(t) \\ 0 & y_{norm_{Batt}}(t) \ge y_{norm_{sc}}(t) \end{cases} \tag{9}$$

The LPF time constant will remain unaltered for $y_{norm_{Batt}}(t) \ge y_{norm_{sc}}(t)$. However, it will gradually increase as battery normalized SOC falls below SC normalized SOC. As a result, the battery discharge rate will not change quickly for any future change in power requirement. Hence, the SC compensates for the additional power while increasing its utilization. If the battery is charged enough, or the SC normalized SOC again falls below that of the battery, the battery discharge rate will be restored to its initial value.

IV. RESULTS AND DISCUSSION

The proposed EMS has been simulated in MATLAB/SIMULINK platform with different power flow conditions for a long duration. The system parameters are shown in Table I. The power profile used in the simulation and corresponding DC link voltage profile is shown in Fig. 6. The

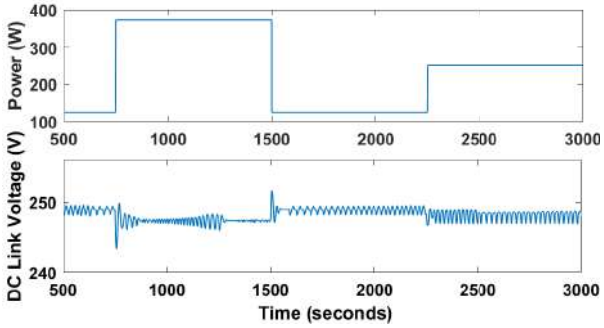

Fig. 6. DC link power and voltage at different power level.

power changes from $P = 124W$ to $P = 373W$ at $t = 750s$, then reduced to $P = 124W$ at $t = 1500s$ and again increased to $P = 250W$ at $t = 2250s$. It can be seen that the DC

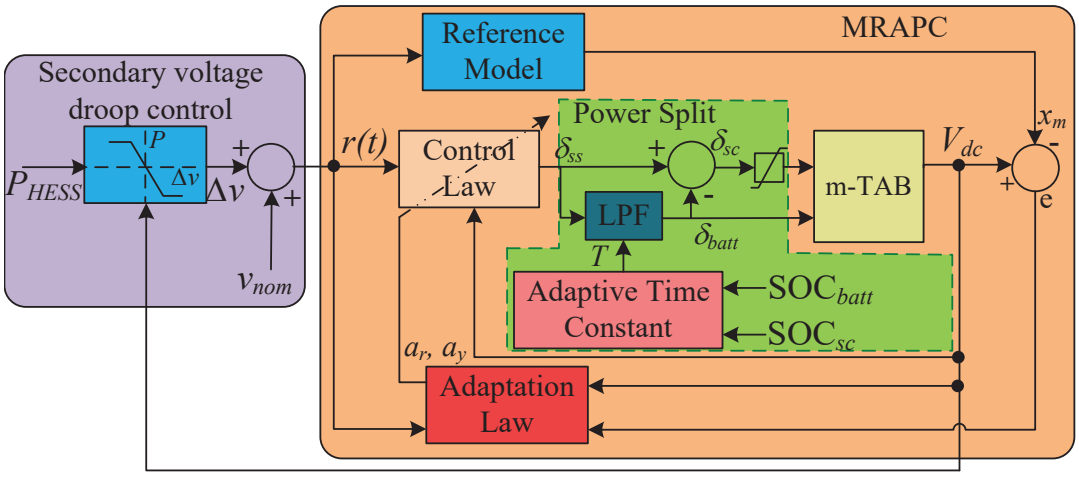

Fig. 4. Control schematic for the m-TAB with SOC based adaptive EMS

link voltage is well within the acceptable 5% of the nominal voltage. The voltage waveforms at the different winding of the HFT at transient and steady states are presented in Fig. 7 and Fig. 8. It can be seen from Fig. 7 that, initially, at the time of step increase in load power from $124W$ to $373W$ at $t = 750s$, the phase shift angle δ_{batt} remains unaltered whereas, δ_{sc} jumps to a new value. Gradually, the δ_{batt} start to increase, and δ_{sc} starts to decrease as per the adaptive power split. At steady state, as shown in Fig. 8, the δ_{batt} attains a new value to meet total power demand, and δ_{sc} is reduced to a value to maintain zero power at the SC port. The power distribution between battery and SC with the conventional and adaptive EMS has been compared and shown in Fig. 9a. It can be seen that initially, the battery discharge rate is the same for both conventional and adaptive EMS algorithms. However, as the battery normalized SOC falls below the SC normalized SOC, the adaptive EMS increases the time constant of the LPF, and the battery discharge rate decreases. Hence, the battery power takes longer to reach the steady state value than the conventional EMS algorithm.

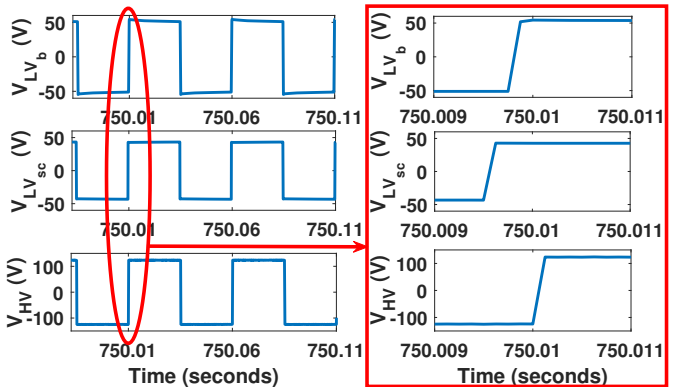

Fig. 7. HFT voltages at transient state.

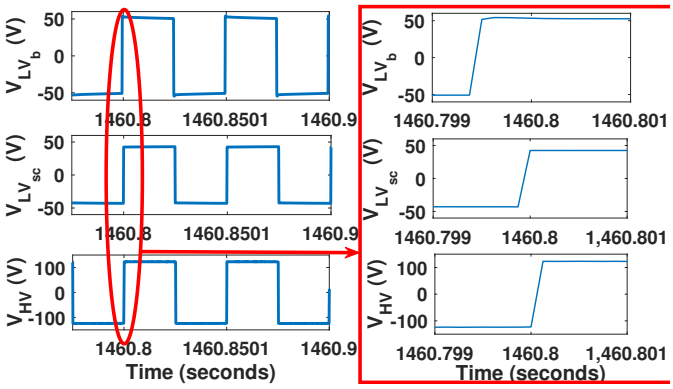

Fig. 8. HFT voltages at steady state.

A comparison of the LPF time constant for conventional and adaptive EMS is shown in Fig. 9b. It also showcases the comparison of δ_{batt} for both cases. It can be seen that for the adaptive EMS, the δ_{batt} change is not sharp as in the case of conventional EMS. A comparison of SC and battery SOC is also drawn in Fig. 10a and 10b, respectively. It can be inferred from Fig. 10 that the SOC of the battery reduces slowly in the case of adaptive EMS as compared to the conventional EMS, thereby proving a reduction in the discharge rate of the battery. During that period, the SC caters to the additional power, and its SOC is reduced at a higher rate with the adaptive EMS.

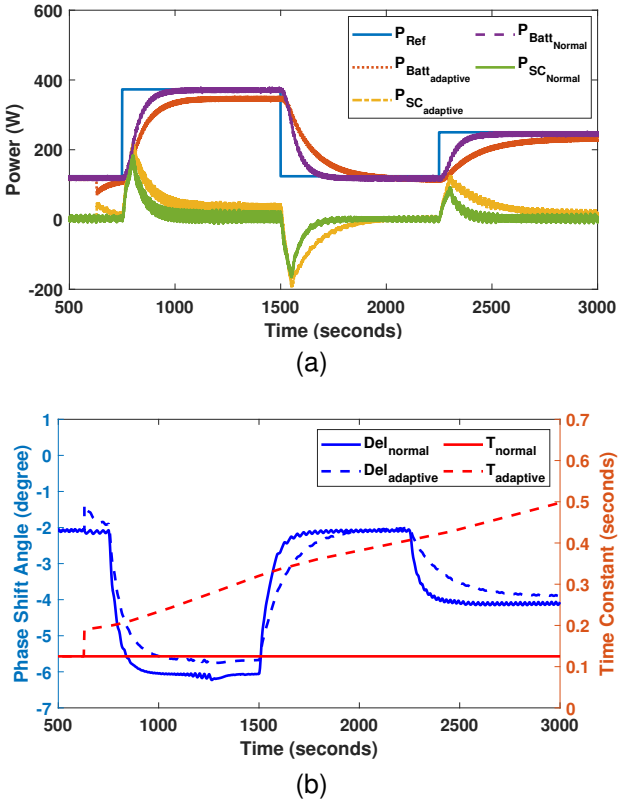

Fig. 9. (a) Power allocation using conventional EMS and SOC based adaptive EMS, (b) phase shift angle and time constant of LPF with conventional EMS and SOC based adaptive EMS.

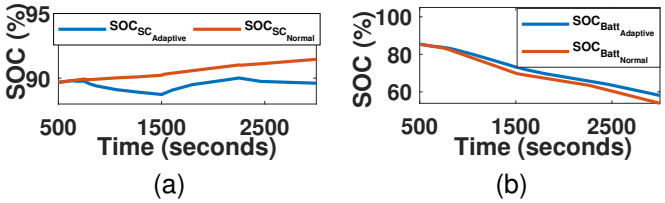

Fig. 10. (a) SOC of SC under conventional and adaptive condition, (b) SOC of battery under conventional and adaptive condition.

A laboratory-developed m-TAB experimental prototype is depicted in Fig. 11. The system parameters are the same as given in Table I. The LV side and NPC side bridges are developed using TK56A12N1 and IXFP38N30X3M MOSFETs, respectively. Isolated gate drivers ISO5452DW have been used to trigger the MOSFETs. The complete control method is coded in the TMS320F28379D evaluation board.

The voltage has been sensed using TLV9062 operational amplifier and AMC1311DWVR isolated amplifier. One of the H-bridge is connected to a LiFePO4 battery with a nominal voltage of 48V and a capacity of 10Ah. The other H-bridge is connected to three series-connected super-capacitor of rating 58F-16.8V. From the measured voltage and currents, the SOCs of the ESDs are estimated. However, the details of the SOC

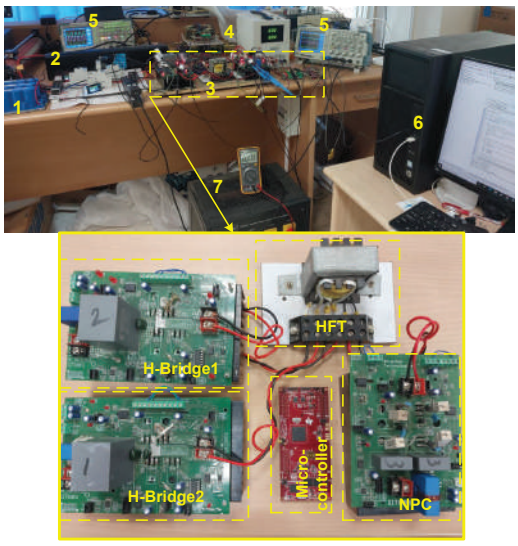

Fig. 11. Experimental setup (1) SC, (2) Battery, (3) m-TAB, (4) Power supply, (5) DSO, (6) Computer interface, (7) Load.

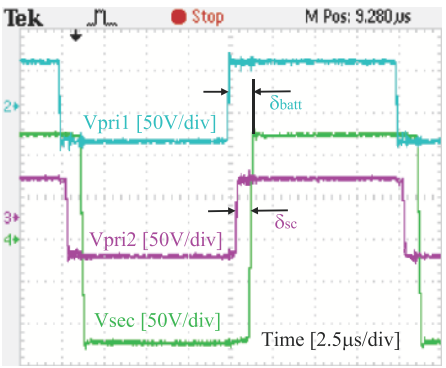

(a)

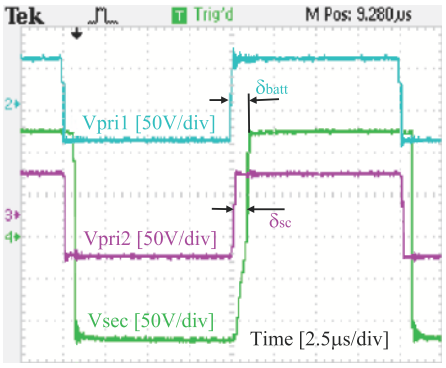

(b)

Fig. 12. HFT voltage waveforms at steady state for (a) $P = 373W$ (b) $P = 124W$.

estimation are not in this manuscript's scope and have been left out.

The effect of different power flow at different SOC level has been verified in the experimental setup. The steady-state voltages at the high-frequency transformer's three ports are depicted in Fig 12. The overall testing is divided into sub-parts as described below.

A. Short term analysis

1) Case I: In this case, both the ESD was started with full charge condition, and the effect of power flow changes are observed and shown in Fig. 13. For a power variation from $124W$ to $373W$, the power allocation between the battery and SC is shown in Fig. 13a. It is observed that, during a power rise, the battery current reaches the steady state values in 10s as desired. Fig. 13b and Fig. 13c show both power rise and fall conditions at different level of power. As seen from them,

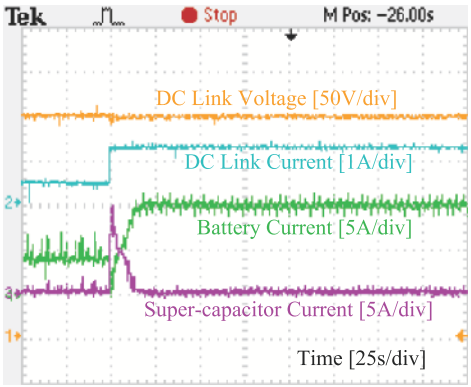

(a)

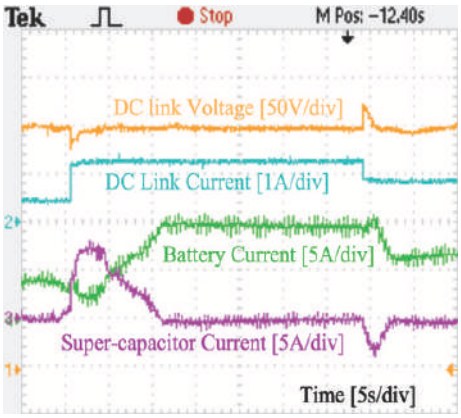

(b)

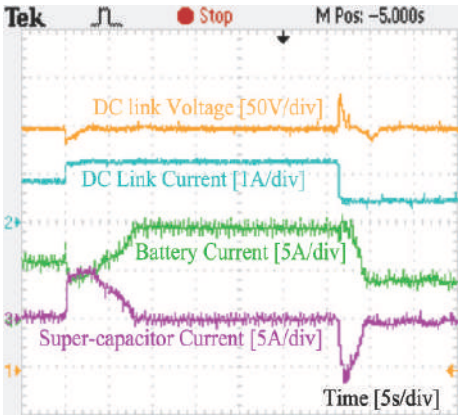

(c)

Fig. 13. DC link voltage, DC link current, battery current and SC current in case I for (a) $P = 124W \rightarrow P = 373W$, (b) $P = 124W \rightarrow P = 373W \rightarrow P = 250W$, (c) $P = 250W \rightarrow P = 373W \rightarrow P = 124W$.

in all cases, the power allocation takes 10s to achieve a steady state condition during power rise, while it takes only 2s during power fall.

2) Case II: In this case, the ESDs were started with different values of the SOCs. Initially, battery SOC was 60%, whereas that of SC was 75%. Hence, the time constant of the LPF is increased by the controller, and the effect of change in power flow is shown in Fig. 14. It can be seen from Fig. 14a that for the same variation of power from $124W$ to $373W$, the battery current reaches the steady state value in 15s. Fig. 14b shows the effect of power rise and fall in this scenario.

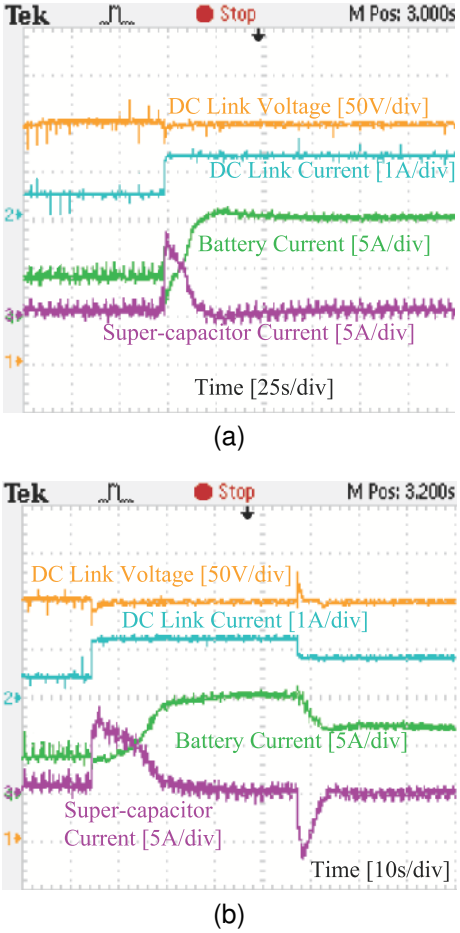

Fig. 14. DC link voltage, DC link current, battery current and SC current in case II for (a) $P = 124W \rightarrow P = 373W$, (b) $P = 124W \rightarrow P = 373W \rightarrow P = 250W$.

B. Long term analysis

The proposed techniques are also compared with the conventional method experimentally for a long-time scenario with the power profile as shown in Fig. 15. The corresponding battery and super-capacitor voltage, current, and SOC is shown in Fig. 16 and Fig. 17 respectively. The experiment is started with 85% SOC for the battery and 90% SOC for the super-capacitor. The initial power flow was kept at $124W$ and then changed to $250W \rightarrow 373W \rightarrow 248W$. At the initial stage, the normalized SOC of the super-capacitor is greater than the battery. Hence, the time constant of the LPF is incremented by the proposed adaptive EMS. As a result, the battery current

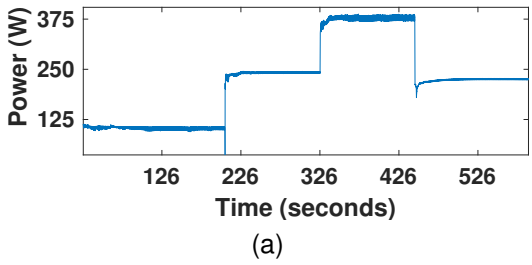

Fig. 15. Power profile for long term experimental analysis.

increases at a slower rate than the conventional method, as shown in Fig. 16b. Similarly, the super-capacitor current decrement is slower in the case of proposed EMS than in the conventional technique, as shown in fig. 17b. A comparison

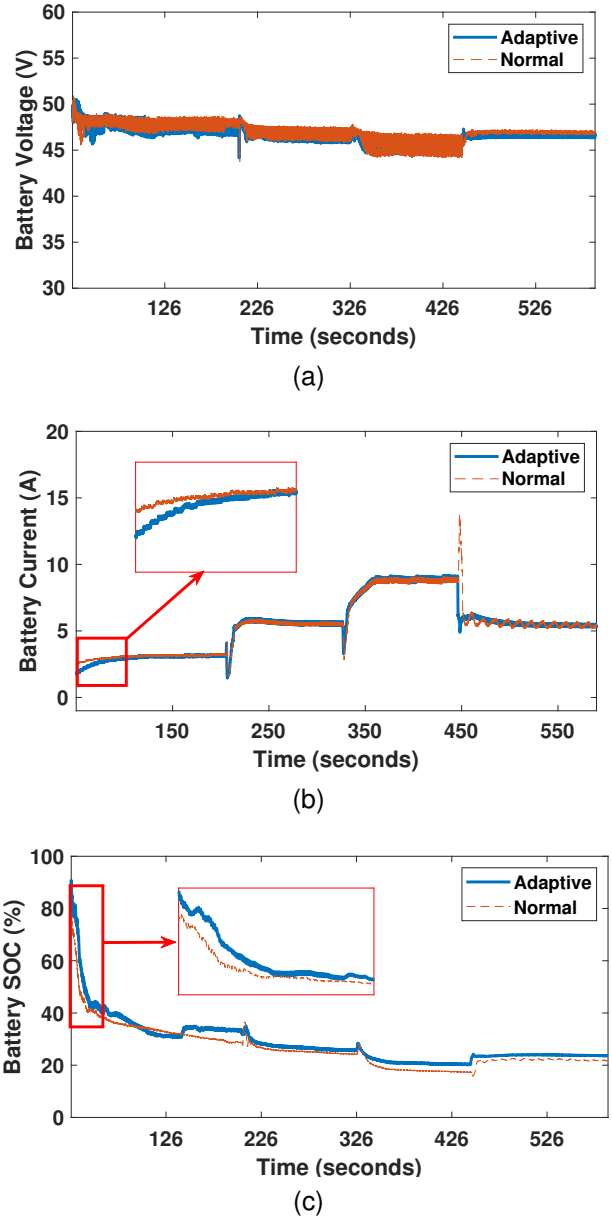

Fig. 16. Long term experimental result comparison for (a) battery voltage, (b) battery current, (c) battery SOC.

is also made between the conventional and proposed methods to show the effect on the SOCs of the ESDs. It is observed that the battery SOC varies slowly, whereas the SOC of the super-capacitor varies faster at the start for adaptive EMS. At the later stage, the normalized SOC of the battery is greater than the super-capacitor, and hence, the current variations are the same for both conventional and adaptive EMS. The experimental results prove the practicability of the proposed adaptive EMS.

V. CONCLUSION

This manuscript presents an efficient adaptive energy management system for a modified triple active bridge converter-based hybrid energy storage system. The m-TAB provides galvanic isolation between all the ports. The adaptive EMS ensures the individual port power flow control. The SOC-based power split technique dynamically distributes the high and low-frequency components of power demand. The adaptive EMS monitors the capacity of the energy storage devices during the operation and estimates a suitable time constant for the LPF to distribute the power between the storage devices. The adaptive feature of the proposed EMS changes the discharge rate of the battery as per the system condition, reduces battery stress, and improves its lifetime. The system has been simulated in the MATLAB/SIMULINK environment to verify the adaptive EMS algorithm for different power flow conditions. A comparison with the conventional approach is also presented to corroborate the superiority of the proposed technique. Finally, experimentation on a 500W hardware prototype has also been performed, and the results are furnished with different short-term and long-term test scenarios to support the real-time application of the proposed system.

In future work, the proposed adaptive EMS could be modified to consider other states of health parameters of the ESDs to determine the power allocation ratio. In this way, the ESD stress can be further minimized, and its life cycle could be improved. In addition to that, the performance of the adaptive EMS could be investigated for uncertain disturbances, faults, and system conditions.

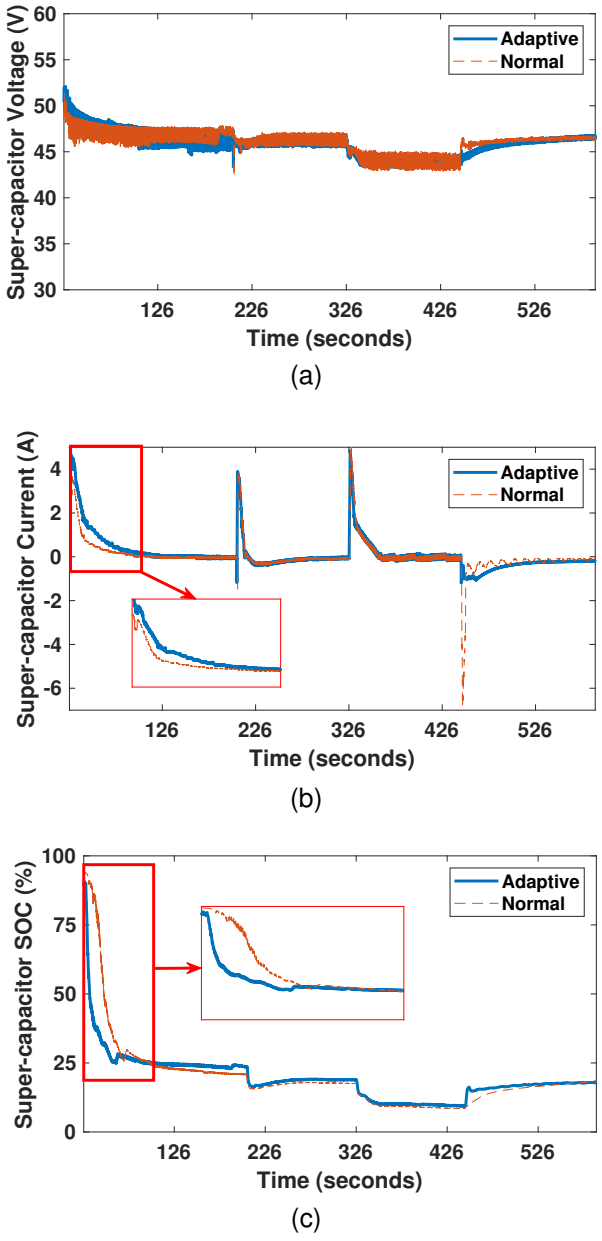

Fig. 17. Long term experimental result comparison for (a) super-capacitor voltage, (b) super-capacitor current, (c) super-capacitor SOC.

REFERENCES

[1] B. Ćosić, G. Krajačić, and N. Duić, "A 100the year 2050: The case of macedonia," *Energy*, vol. 48, no. 1, pp. 80 – 87, 2012, 6th Dubrovnik Conference on Sustainable Development of Energy Water and Environmental Systems, SDEWES 2011. [Online]. Available: http://www.sciencedirect.com/science/article/pii/S0360544212005300

[2] G. Pleßmann, M. Erdmann, M. Hlusiak, and C. Breyer, "Global energy storage demand for a 100% renewable electricity supply," *Energy Procedia*, vol. 46, no. 0, pp. 22–31, 2014.

[3] M. Bazilian, T. Mai, S. Baldwin, D. Arent, M. Miller, and J. Logan, "Decision-making for high renewable electricity futures in the united states," *Energy Strategy Reviews*, vol. 2, no. 3-4, pp. 326–328, 2014.

[4] P. D. Lund, J. Lindgren, J. Mikkola, and J. Salpakari, "Review of energy system flexibility measures to enable high levels of variable renewable electricity," *Renewable and Sustainable Energy Reviews*, vol. 45, pp. 785–807, 2015.

[5] A. S. Brouwer, M. Van Den Broek, A. Seebregts, and A. Faaij, "Impacts of large-scale intermittent renewable energy sources on electricity systems, and how these can be modeled," *Renewable and Sustainable Energy Reviews*, vol. 33, pp. 443–466, 2014.

[6] S. Weitemeyer, D. Kleinhans, T. Vogt, and C. Agert, "Integration of renewable energy sources in future power systems: The role of storage," *Renewable Energy*, vol. 75, pp. 14–20, 2015.

[7] M. F. Romlie, M. Rashed, C. Klumpner, and G. M. Asher, "An analysis of efficiency improvement with the installation of energy storage in power systems," in *7th IET International Conference on Power Electronics, Machines and Drives (PEMD 2014)*, 2014, pp. 1–6.

[8] K. Raviteja, P. K. Kar, and S. B. Karanki, "Renewable energy resources integration to grid with improved power quality capabilities and optimal power flows," in *2018 IEEE International Conference on Power Electronics, Drives and Energy Systems (PEDES)*. IEEE, 2018, pp. 1–6.

[9] J. Rocabert, R. Capo-Misut, R. S. Munoz-Aguilar, J. I. Candela, and P. Rodriguez, "Control of energy storage system integrating electrochemical batteries and supercapacitors for grid-connected applications," *IEEE Transactions on Industry Applications*, vol. 55, no. 2, pp. 1853–1862, 2018.

[10] Z. Amjadi and S. S. Williamson, "Modeling, simulation, and control of an advanced luo converter for plug-in hybrid electric vehicle energy-storage system," *IEEE Transactions on Vehicular Technology*, vol. 60, no. 1, pp. 64–75, 2011.

[11] S. Inoue and H. Akagi, "A bidirectional dc–dc converter for an energy storage system with galvanic isolation," *IEEE Transactions on Power Electronics*, vol. 22, no. 6, pp. 2299–2306, 2007.
[12] H. Tao, A. Kotsopoulos, J. L. Duarte, and M. A. Hendrix, "Family of multiport bidirectional dc–dc converters," *IEE Proceedings-Electric Power Applications*, vol. 153, no. 3, pp. 451–458, 2006.
[13] C. Zhao, S. D. Round, and J. W. Kolar, "An isolated three-port bidirectional dc-dc converter with decoupled power flow management," *IEEE transactions on power electronics*, vol. 23, no. 5, pp. 2443–2453, 2008.
[14] Z. Ling, H. Wang, K. Yan, and J. Gan, "Optimal isolation control of three-port active converters as a combined charger for electric vehicles," *Energies*, vol. 9, no. 9, p. 715, 2016.
[15] D.-D. Nguyen, G. Fujita, and M. C. Ta, "A new soft-switching strategy for three-port converter to be applied in ev application," in *2017 IEEE 3rd International Future Energy Electronics Conference and ECCE Asia (IFEEC 2017-ECCE Asia)*. IEEE, 2017, pp. 1126–1131.
[16] V. Nair, S. Gulur, R. Chattopadhyay, and S. Bhattacharya, "Integrating photovoltaics and battery energy storage to grid using triple active bridge and voltage source converters," in *IECON 2020 The 46th Annual Conference of the IEEE Industrial Electronics Society*. IEEE, 2020, pp. 3691–3696.
[17] I. Biswas, D. Kastha, and P. Bajpai, "Small signal modeling and decoupled controller design for a triple active bridge multiport dc–dc converter," *IEEE Transactions on Power Electronics*, vol. 36, no. 2, pp. 1856–1869, 2020.
[18] M. Phattanasak, R. Gavagsaz-Ghoachani, J.-P. Martin, S. Pierfederici, and B. Davat, "Flatness based control of an isolated three-port bidirectional dc-dc converter for a fuel cell hybrid source," in *2011 IEEE Energy Conversion Congress and Exposition*. IEEE, 2011, pp. 977–984.
[19] P. Thounthong, M. Phattanasak, P. Sethakul, J. . Martin, S. Pierfederici, and B. Davat, "Nonlinear control of a magnetic coupling converter for a supercapacitor storage device for a dc link stabilization," in *2013 International Conference on Clean Electrical Power (ICCEP)*, 2013, pp. 645–652.
[20] S. K. Mitra and S. B. Karanki, "A grid integrated bi-directional dual active bridge converter with model reference adaptive control based power flow controller," in *2019 National Power Electronics Conference (NPEC)*. IEEE, 2019, pp. 1–5.
[21] S. M. Rezvanizaniani, Z. Liu, Y. Chen, and J. Lee, "Review and recent advances in battery health monitoring and prognostics technologies for electric vehicle (ev) safety and mobility," *Journal of power sources*, vol. 256, pp. 110–124, 2014.
[22] G. Ning, B. Haran, and B. N. Popov, "Capacity fade study of lithium-ion batteries cycled at high discharge rates," *Journal of power sources*, vol. 117, no. 1-2, pp. 160–169, 2003.
[23] H. Tao, A. Kotsopoulos, J. Duarte, and M. Hendrix, "A soft-switched three-port bidirectional converter for fuel cell and supercapacitor applications," in *2005 IEEE 36th Power Electronics Specialists Conference*. IEEE, 2005, pp. 2487–2493.
[24] H. Li and D. Liu, "Power distribution strategy of fuel cell vehicle system with hybrid energy storage elements using triple half bridge (thb) bidirectional dc-dc converter," in *2007 IEEE Industry Applications Annual Meeting*. IEEE, 2007, pp. 636–642.
[25] K. Wang, X. Liu, L. Zhao, Y. Zhou, and D. Xu, "Research on structure and energy management strategy of household energy router based on hybrid energy storage," in *2019 IEEE Power & Energy Society Innovative Smart Grid Technologies Conference (ISGT)*. IEEE, 2019, pp. 1–5.
[26] E. De Din, H. A. B. Siddique, M. Cupelli, A. Monti, and R. W. De Doncker, "Voltage control of parallel-connected dual-active bridge converters for shipboard applications," *IEEE Journal of Emerging and Selected Topics in Power Electronics*, vol. 6, no. 2, pp. 664–673, 2017.
[27] M. Rolak, C. Sobol, M. Malinowski, and S. Stynski, "Efficiency optimization of two dual active bridge converters operating in parallel," *IEEE Transactions on Power Electronics*, vol. 35, no. 6, pp. 6523–6532, 2019.
[28] M. M. S. Khan, M. O. Faruque, and A. Newaz, "Fuzzy logic based energy storage management system for mvdc power system of all electric ship," *IEEE Transactions on Energy Conversion*, vol. 32, no. 2, pp. 798–809, 2017.
[29] G. Buticchi, L. F. Costa, D. Barater, M. Liserre, and E. D. Amarillo, "A quadruple active bridge converter for the storage integration on the more electric aircraft," *IEEE Transactions on Power Electronics*, vol. 33, no. 9, pp. 8174–8186, 2017.
[30] Y. Zhou, Z. Huang, H. Liao, H. Li, Y. Jiao, and J. Peng, "A predictive set-point modulation energy management strategy for hybrid energy storage systems," *IEEE Transactions on Industry Applications*, vol. 55, no. 6, pp. 6266–6277, 2019.
[31] A. Florescu, S. Bacha, I. Munteanu, A. I. Bratcu, and A. Rumeau, "Adaptive frequency-separation-based energy management system for electric vehicles," *Journal of Power Sources*, vol. 280, pp. 410–421, 2015.
[32] T. Wu, W. Yu, and L. Guo, "A study on use of hybrid energy storage system along with variable filter time constant to smooth dc power fluctuation in microgrid," *IEEE Access*, vol. 7, pp. 175 377–175 385, 2019.
[33] H. Liao, J. Peng, Y. Wu, H. Li, Y. Zhou, X. Zhang, and Z. Huang, "Adaptive split-frequency quantitative power allocation for hybrid energy storage systems," *IEEE Transactions on Transportation Electrification*, vol. 7, no. 4, pp. 2306–2317, 2021.
[34] S. K. Mitra and S. B. Karanki, "An soc based adaptive energy management system for hybrid energy storage system integration to grid," in *2021 IEEE 12th Energy Conversion Congress & Exposition-Asia (ECCE-Asia)*. IEEE, 2021, pp. 2034–2039.
[35] J. Hou, J. Sun, and H. F. Hofmann, "Mitigating power fluctuations in electric ship propulsion with hybrid energy storage system: Design and analysis," *IEEE Journal of Oceanic Engineering*, vol. 43, no. 1, pp. 93–107, 2017.